



HAL
open science

Numerical simulations of hydraulic jumps with the Shear Shallow Water model

Argiris I Delis, Hervé Guillard, Yih-Chin Tai

► **To cite this version:**

Argiris I Delis, Hervé Guillard, Yih-Chin Tai. Numerical simulations of hydraulic jumps with the Shear Shallow Water model. [Research Report] RR-9127, INRIA Sophia Antipolis - Méditerranée; UCA, Inria. 2017. hal-01647019

HAL Id: hal-01647019

<https://inria.hal.science/hal-01647019>

Submitted on 24 Nov 2017

HAL is a multi-disciplinary open access archive for the deposit and dissemination of scientific research documents, whether they are published or not. The documents may come from teaching and research institutions in France or abroad, or from public or private research centers.

L'archive ouverte pluridisciplinaire **HAL**, est destinée au dépôt et à la diffusion de documents scientifiques de niveau recherche, publiés ou non, émanant des établissements d'enseignement et de recherche français ou étrangers, des laboratoires publics ou privés.



Numerical simulations of hydraulic jumps with the Shear Shallow Water model

Argiris I. Delis, Hervé Guillard, Yih-Chin Tai

**RESEARCH
REPORT**

N° 9127

November 2017

Project-Team Castor



Numerical simulations of hydraulic jumps with the Shear Shallow Water model

Argiris I. Delis^{*}, Hervé Guillard[†], Yih-Chin Tai[‡]

Project-Team Castor

Research Report n° 9127 — November 2017 — 27 pages

Abstract: An extension and numerical approximation of the shear shallow water equations model recently proposed in [21] is considered in this work. The model equations are able to describe the oscillatory nature of turbulent hydraulic jumps and as such correct the deficiency of the classical shallow water equations in describing such phenomena. The model equations, originally developed for horizontal flow or flows occurring over small constant slopes, are straightforwardly extended here for modeling flows over non-constant slopes and numerically solved by a second-order well-balanced finite volume scheme. Further, a new set of exact solutions to the extended model equations are derived and several numerical tests are performed to validate the numerical scheme and its ability to predict the oscillatory nature of hydraulic jumps under different conditions.

Key-words: Shallow water model, St Venant Equations, Hydraulic jump, Turbulent Hydraulic jump, Free surface flows, Numerical model

^{*} Division of Sciences, School of Production Engineering & Management, Technical University of Crete, 73100 Chania, Crete, Greece, adelis@science.tuc.gr

[†] Inria Sophia Antipolis Méditerranée and Côte d'Azur University, LJAD, CNR, France, herve.guillard@inria.fr

[‡] Department of Hydraulic and Ocean Engineering, National Cheng Kung University, Tainan 701, Taiwan, yctai@mail.ncku.edu.tw

**RESEARCH CENTRE
SOPHIA ANTIPOLIS – MÉDITERRANÉE**

2004 route des Lucioles - BP 93
06902 Sophia Antipolis Cedex

Simulations numériques de ressauts hydrauliques avec un modèle St Venant cisailé

Résumé : Ce travail considère une extension et une approximation numérique du modèle de St Venant cisailé récemment proposé dans [21]. Les équations du modèle peuvent décrire la nature oscillante des ressauts hydrauliques turbulents et ainsi corriger les défauts des équations de St Venant classiques dans la description de tels phénomènes. Les équations du modèle, à l'origine développées pour un écoulement sur fond horizontal ou sur des petites pentes constantes, sont ici étendues pour modéliser des écoulements des pentes non-constantes. Une approximation numérique utilisant un schéma du second ordre de type volume fini bien équilibré est proposée. De plus, un nouvel ensemble de solutions exactes des équations du modèle est construit et plusieurs tests numériques sont présentés pour valider le schéma numérique et sa capacité à calculer la nature oscillante des ressauts hydrauliques sous diverses conditions.

Mots-clés : St Venant Equations, Ressaut hydraulique, Ressaut hydraulique turbulent, Simulations numériques

1 Introduction

Hydraulic jumps are commonly observed in laboratory experiments, river flows or coastal areas. The classical description of this phenomenon uses the shallow water hyperbolic system of equations (SWE) and assimilates hydraulic jumps to a discontinuity of zero length governed by jump relations between the supercritical upstream state and the subcritical downstream one as:

$$\begin{aligned} [h(u - D)] &= 0; \\ [hu(u - D) + gh^2/2] &= 0 \end{aligned} \tag{1}$$

where here $[\cdot]$ stands for the jump $(\cdot)_R - (\cdot)_L$ between the upstream state $(\cdot)_L$ and the downstream one $(\cdot)_R$, h is the water height, u the flow velocity, g the gravity acceleration and D the jump velocity.

This classical description of hydraulic jumps has well-known shortcomings. As observed in many laboratory experiments, see e.g [3], hydraulic jumps have a non-zero width and their shapes are different according to the upstream Froude number. In particular, for large Froude numbers (typically larger than 1.7) the jump becomes turbulent; the water depth rapidly increases, large scale turbulent eddies, forming a roller, appear beneath the free surface and intense vorticity generation is observed. Oscillations with well-defined frequencies of the toe of the hydraulic jump have been also reported [18, 4].

Building on an earlier work devoted to roll waves [20] Richard and Gavriluk have proposed in [21] a new model for turbulent hydraulic jumps, called the Shear Shallow Water Equations (SSWE), that attempt to correct most of the deficiencies of the classical shallow water description of these phenomena. In particular, their model is able to compute the jump's toe oscillations with a frequency that compare reasonably well with the experiments. This model is also interesting since it contains only two adjustable parameters with a well-defined physical interpretations. These two parameters, the wall enstrophy ϕ and the energy dissipation coefficient C_r have been determined in Richard and Gavriluk's model from the experiments by Hager and Bremen [10].

The model of [21] has been developed for horizontal flows or flows occurring on a small constant slope. The purpose of this work is to investigate a straightforward extension of this model for flows on non-constant slopes. In particular, no attempts have been made to adjust the parameters of the model to this new situation and we have used the values given in [21].

The remainder of this paper is the following: In Section 2, we recall some salient features of the model proposed in [21] and describe its extension for flows over a non-constant topography. Then, in Section 3, we describe the numerical method used to approximate the solutions of the model. Actually, the model of [21] is a conservative hyperbolic system with a stiff source term whose approximation is not straightforward. The design of a second-order (in space and time) finite volume numerical scheme used for its extension on non-constant topography necessitates to integrate some modifications related to the preservation of equilibrium (lake at rest) solutions. In this last section, we present some numerical tests and corresponding results. Some new analytical solutions of the SSWE over non-constant topography are derived, by modifying some well-known benchmark cases used in shallow water studies. Finally, a numerical comparison with experimental data from a forced hydraulic jump is also presented.

2 The shear shallow water model

We recast here the SSWE of [21] as to incorporate a space varying bottom topography, $b \equiv b(x)$, written in one-dimensional conservative form as

$$\partial_t \mathbf{U} + \partial_x \mathbf{F}(\mathbf{U}) = \mathbf{S}_b + \mathbf{S}_f, \quad (2)$$

where the vectors of conserved variables \mathbf{U} , fluxes \mathbf{F} and source terms \mathbf{S}_b and \mathbf{S}_f are defined as

$$\mathbf{U} = \begin{pmatrix} h \\ q \\ E \end{pmatrix}, \quad \mathbf{F} = \begin{pmatrix} q \\ \frac{q^2}{h} + P \\ q(E+P)/h \end{pmatrix}, \quad \mathbf{S}_b = \begin{pmatrix} 0 \\ -gh\partial_x b \\ 0 \end{pmatrix}, \quad \mathbf{S}_f = \begin{pmatrix} 0 \\ -C_f \frac{|q|q}{h^2} \\ -\left(C_f + C_r \frac{\Phi - \phi_s}{\Phi}\right) \frac{|q|^3}{h^3} \end{pmatrix} \quad (3)$$

with h being the water depth, $q = hu$ the unit discharge, u the average velocity and E is the total energy defined as

$$E = h \frac{u^2}{2} + g \frac{h^2}{2} + ghb + \Phi \frac{h^3}{2}$$

In this relation, the first two term represents respectively the kinetic and potential energies while the last one stands for a turbulent energy defined thanks to the total enstrophy Φ . For details on the physical interpretation of the model, we refer to [21]. P the pressure is given as

$$P = \frac{gh^2}{2} + \Phi h^3.$$

Further, defining an "internal energy" e by

$$e = \frac{gh}{2} + gb + \Phi \frac{h^2}{2}$$

the following equation of state is verified

$$P = 2he - \frac{gh^2}{2} - 2ghb = 2E - hu^2 - \frac{gh^2}{2} - 2ghb.$$

The two source terms \mathbf{S}_b and \mathbf{S}_f stand respectively for the topography and the friction terms. In the latter, C_f is the friction coefficient, related to the Darcy-Weisbach coefficient f by $C_f = f/8$ and C_r is a drag coefficient corresponding to the dissipation of the enstrophy in the turbulent roller generated in an hydraulic jump. Further, the total enstrophy is decomposed as

$$\Phi = \Psi + \phi_s$$

where ϕ_s is the small scale enstrophy describing the intensity of the vortices in the boundary layer near the bed, and Ψ is the large scale (roller) enstrophy. It can be seen that system (2) implies the following equation for the enstrophy

$$\partial_t \Phi + u \partial_x \Phi = -\frac{2}{h^3} C_r \frac{\Phi - \phi_s}{\Phi} |u|^3. \quad (4)$$

System (2) admits the following quasi-linear form, setting $\mathbf{W} = (h, u, \Phi)^T$,

$$\partial_t \mathbf{W} + \mathbf{A} \partial_x \mathbf{W} = \tilde{\mathbf{S}}_b + \tilde{\mathbf{S}}_f$$

where

$$\mathbf{A} = \begin{pmatrix} u & h & 0 \\ g + 3h\Phi & u & h^2 \\ 0 & 0 & u \end{pmatrix}, \quad \tilde{\mathbf{S}}_b = \begin{pmatrix} 0 \\ -g\partial_x b \\ 0 \end{pmatrix}, \quad \tilde{\mathbf{S}}_f = \begin{pmatrix} 0 \\ -C_f \frac{|u|u}{h} \\ -\frac{2}{h^3} C_r \frac{\Phi - \phi_s}{\Phi} |u|^3 \end{pmatrix}.$$

The characteristic polynomial of \mathbf{A} is then given as

$$\chi(\mathbf{A}) = (u - \lambda) ((u - \lambda)^2 - (gh + 3\Phi h^2))$$

with roots $\lambda_1 = u - \alpha$, $\lambda_2 = u$, $\lambda_3 = u + \alpha$ where $\alpha = \sqrt{gh + 3\Phi h^2}$, verifying the hyperbolic nature of system (2).

An important property of (2), related to the source terms, is that admits non-trivial steady-states. Following from (2) these may be given as

$$\begin{aligned} \partial_x q &= 0 \\ q\partial_x u + gh\partial_x(h + b) + \partial_x(\Phi h^3) &= -C_f \frac{|q|q}{h^2} \\ \partial_x(u(E + P)) &= -\frac{2}{h^3} C_r \frac{\Phi - \phi_s}{\Phi} \frac{|q|^3}{h^3} \end{aligned}$$

From the above equilibria some classes of steady-state solutions can be derived which can help to assess the performance of a numerical scheme and will be considered later on in Section 4.3.

An important elementary solution is the so-called flow at rest that is easily obtained assuming $u = q = 0$ and $h + b = \eta(x, 0) = \eta_0$ (constant). For the SSWE we see that from the momentum equation a steady equilibrium is obtained in this case if the enstrophy verifies also

$$\partial_x(\Phi h^3) = 0$$

This relation is verified if $\Phi = 0$ that is consistent with the physical requirement that no large or small scale enstrophy is created in the stagnant water case. Therefore $\mathbf{W}_0 = (\eta_0 - b, 0, 0)^t$ defines a class of exact steady solution of the model.

3 Numerical method

We describe here a relatively simple finite volume (FV) scheme for system (2) that is of second-order accuracy in space and time and is well-balanced in the sense of preserving exactly the flow at rest solution thus allowing to have an efficient treatment of the topography source term. In practice, schemes preserving this equilibrium give good results even in unsteady cases. In this FV scheme a splitting method is adopted where at the first step we solve the system of equations without the drag term \mathbf{S}_f and the well-balanced spatial discretization is utilized. At the second step in the splitting method, we take into account the friction term and a system of ordinary equations is to be solved. For this, we will use the fact that due to the special structure of system (2) these odes can be solved in an exact way.

3.1 Advection step and well-balancing

At the first step of the splitting, we consider the following semi-discrete form of the FV scheme for the convection terms and topography source term \mathbf{S}_b

$$\Delta x \partial_t \mathbf{U}_i + \mathbf{F}_{i+1/2} - \mathbf{F}_{i-1/2} = \mathbf{S}_b^{i+1/2} + \mathbf{S}_b^{i-1/2} \quad (5)$$

where $i = 1, \dots, N$ refers to the center of the computational cell $I_i = [x_{i-1/2}, x_{i+1/2}] = [x_i - \frac{1}{2}\Delta x, x_i + \frac{1}{2}\Delta x]$, $\mathbf{F}_{i\pm 1/2}$ are the numerical fluxes at the cell's interfaces $i \pm 1/2$. To design the topography source terms discretisations at the cell interfaces, $\mathbf{S}_b^{i\pm 1/2}$, we need to specify first the form of the numerical fluxes. In this work, we consider the Rusanov numerical flux which writes as

$$\mathbf{F}_{i+1/2} = \frac{1}{2} \left(\mathbf{F}(\mathbf{U}_{i+1/2}^R) + \mathbf{F}(\mathbf{U}_{i+1/2}^L) \right) - \frac{\mathcal{C}_{i+1/2}}{2} \left(\mathbf{U}_{i+1/2}^R - \mathbf{U}_{i+1/2}^L \right) \quad (6)$$

where $(\cdot)_{i+1/2}^L$ and $(\cdot)_{i+1/2}^R$ denote the left and right (possibly reconstructed) solution and topography values at the $i + 1/2$ interface and

$$\mathcal{C}_{i+1/2} = \sup_{\mathbf{U} = \mathbf{U}_{i+1/2}^{R,L}} \left(\sup_{j=1,2,3} |\lambda_j(\mathbf{U})| \right)$$

with λ_j being the eigenvalues of the system. For a first order spatial scheme one has $\mathbf{U}_{i+1/2}^R = \mathbf{U}_{i+1}$ and $\mathbf{U}_{i+1/2}^L = \mathbf{U}_i$.

Now, plugging the numerical flux expression (6) in the scheme (5) and after some simple manipulations, we can write it in the following fluctuation form

$$\begin{aligned} \Delta x \partial_t \mathbf{U}_i &+ \frac{1}{2} \left(\mathbf{F}(\mathbf{U}_{i+1/2}^R) - \mathbf{F}(\mathbf{U}_{i+1/2}^L) \right) + \mathbf{F}(\mathbf{U}_{i+1/2}^L) - \mathbf{F}(\mathbf{U}_i) - \frac{\mathcal{C}_{i+1/2}}{2} \left(\mathbf{U}_{i+1/2}^R - \mathbf{U}_{i+1/2}^L \right) \\ &+ \frac{1}{2} \left(\mathbf{F}(\mathbf{U}_{i-1/2}^R) - \mathbf{F}(\mathbf{U}_{i-1/2}^L) \right) - \mathbf{F}(\mathbf{U}_{i-1/2}^R) + \mathbf{F}(\mathbf{U}_i) + \frac{\mathcal{C}_{i-1/2}}{2} \left(\mathbf{U}_{i-1/2}^R - \mathbf{U}_{i-1/2}^L \right) \\ &= \mathbf{S}_b^{i+1/2} + \mathbf{S}_b^{i-1/2}. \end{aligned}$$

For the flow at rest equilibrium the above scheme takes the following form by setting $\partial_t \mathbf{U}_i = 0$ and $u = q = 0$

$$\begin{aligned} &\frac{1}{2} \begin{pmatrix} 0 \\ g\bar{h}_{i+1/2} \Delta h_{i+1/2} \\ 0 \end{pmatrix} - \begin{pmatrix} 0 \\ g\bar{h}_{i+1/2}^- \Delta h_{i+1/2}^- \\ 0 \end{pmatrix} - \frac{\mathcal{C}_{i+1/2}}{2} \begin{pmatrix} \Delta h_{i+1/2} \\ 0 \\ g\bar{b}_{i+1/2} \Delta h_{i+1/2} \end{pmatrix} \\ &+ \frac{1}{2} \begin{pmatrix} 0 \\ g\bar{h}_{i-1/2} \Delta h_{i-1/2} \\ 0 \end{pmatrix} + \begin{pmatrix} 0 \\ g\bar{h}_{i-1/2}^+ \Delta h_{i-1/2}^+ \\ 0 \end{pmatrix} + \frac{\mathcal{C}_{i-1/2}}{2} \begin{pmatrix} \Delta h_{i-1/2} \\ 0 \\ g\bar{b}_{i-1/2} \Delta h_{i-1/2} \end{pmatrix} \\ &= \mathbf{S}_b^{i+1/2} + \mathbf{S}_b^{i-1/2} \end{aligned}$$

where the following simple notations have been used

$$\bar{(\cdot)}_{i\pm 1/2} = \frac{(\cdot)_{i\pm 1/2}^R + (\cdot)_{i\pm 1/2}^L}{2}, \quad \bar{(\cdot)}_{i+1/2}^- = \frac{(\cdot)_i + (\cdot)_{i+1/2}^L}{2}, \quad \bar{(\cdot)}_{i+1/2}^+ = \frac{(\cdot)_{i+1} + (\cdot)_{i+1/2}^R}{2}$$

and

$$\Delta(\cdot)_{i\pm 1/2} = (\cdot)_{i\pm 1/2}^R - (\cdot)_{i\pm 1/2}^L, \quad \Delta(\cdot)_{i+1/2}^- = (\cdot)_i - (\cdot)_{i+1/2}^L, \quad \Delta(\cdot)_{i+1/2}^+ = (\cdot)_{i+1} - (\cdot)_{i+1/2}^R.$$

We note that for a first order scheme and following from the above notation the terms $g\bar{h}_{i+1/2}^- \Delta h_{i+1/2}^-$ and $g\bar{h}_{i-1/2}^+ \Delta h_{i-1/2}^+$ vanish.

Now, the simplest definition of the discrete source terms, guaranteeing that well-balancedness, is achieved are the following

$$\begin{aligned} \mathbf{S}_b^{i+1/2} + \mathbf{S}_b^{i-1/2} = & \\ & - \frac{1}{2} \begin{pmatrix} 0 \\ g\bar{h}_{i+1/2}\Delta b_{i+1/2} \\ 0 \end{pmatrix} + \begin{pmatrix} 0 \\ g\bar{h}_{i+1/2}^-\Delta b_{i+1/2}^- \\ 0 \end{pmatrix} + \frac{C_{i+1/2}}{2} \begin{pmatrix} \Delta b_{i+1/2} \\ 0 \\ g\bar{b}_{i+1/2}\Delta b_{i+1/2} \end{pmatrix} \\ & - \frac{1}{2} \begin{pmatrix} 0 \\ g\bar{h}_{i-1/2}\Delta b_{i-1/2} \\ 0 \end{pmatrix} - \begin{pmatrix} 0 \\ g\bar{h}_{i-1/2}^+\Delta b_{i-1/2}^+ \\ 0 \end{pmatrix} - \frac{C_{i-1/2}}{2} \begin{pmatrix} \Delta b_{i-1/2} \\ 0 \\ g\bar{b}_{i-1/2}\Delta b_{i-1/2} \end{pmatrix}. \end{aligned}$$

The above discretization exactly preserves the hydrostatic conditions by enforcing at a cell interface that $\Delta h = -\Delta b$, while the terms $g\bar{h}_{i+1/2}^-\Delta b_{i+1/2}^-$ and $g\bar{h}_{i-1/2}^+\Delta b_{i-1/2}^+$, which vanish for a first order scheme, enforce the hydrostatic condition by satisfying $\Delta h^\pm = -\Delta b^\pm$.

3.2 Friction and drag terms treatment

Concerning the treatment of the source term \mathbf{S}_f , at the second splitting step, we use (7) as a prediction without the friction and drag terms, i.e.

$$\mathbf{U}_i^* = \mathbf{U}_i^n - \frac{\Delta t^n}{\Delta x} \left(\mathbf{F}_{i+1/2} - \mathbf{F}_{i-1/2} + \mathbf{S}_b^{i+1/2} + \mathbf{S}_b^{i-1/2} \right) \quad (7)$$

where for simplicity the forward Euler time stepping is presented with Δt^n being the current time step and \mathbf{U}_i^n the average value at time t^n . At the second splitting step the following system of ODEs has to be solved

$$\frac{d\mathbf{U}}{dt} = \mathbf{S}_f(\mathbf{U})$$

with initial condition \mathbf{U}_i^* calculated at the first step. Using the same strategy than in [21], the first two equations of the system can be explicitly solved in each cell I_i as

$$h_i^{n+1} = h_i^*, \quad q_i^{n+1} = \frac{q_i^*}{1 + \Delta t^n |q_i^*| \frac{C_f}{(h_i^*)^2}}. \quad (8)$$

The last equation for the energy, following from (4), is then

$$\frac{d\Psi_i}{dt} = -\frac{2C_r\Psi_i}{\Psi_i + \phi_s} \left(\frac{q_i}{h_i} \right)^3.$$

Integrating it, Ψ_i^{n+1} can be found in implicit form:

$$\Psi_i^{n+1} - \Psi_i^* + \phi_s \ln \left(\frac{\Psi_i^{n+1}}{\Psi_i^*} \right) = \frac{C_r}{C_f} \left(\frac{q_i^*}{(h_i^*)^2} \right)^2 \left(\frac{1}{\left(1 + \Delta t^n |q_i^*| \frac{C_f}{(h_i^*)^2} \right)^2} - 1 \right)$$

which is then solved by the Newton-Raphson method.

3.3 Higher-order spatial and temporal discretizations

As it was mentioned in Section 3.1 a second-order spatial discretization can be obtained by properly define the left and right states at a cell I_i interface. To this end, we utilize the classical MUSCL reconstruction technique, we refer for example in [22], which provides the following states at a cell interface for each of the components of \mathbf{U}_i as.

$$u_{i+1/2}^L = u_i + 0.5s(r_i)(u_i - u_{i-1}), \quad u_{i+1/2}^R = u_{i+1} - 0.5s(r_{i+1})(u_{i+1} - u_i),$$

where

$$r_i = \frac{u_i - u_{i-1}}{u_{i+1} - u_i}$$

and $s(r_i)$ is a limiter function. In the present work the classical Van Leer slope limiter has been utilized in the numerical results presented later on in Section 4.

To achieve second-order accuracy in time the optimal, in the sense of the CFL condition, second-order two-stage Strong Stability Preserving (SSP) Runge-Kutta (RK) method has been implemented. This reads as follows

$$\begin{aligned} \mathbf{U}_i^{(1)} &= \mathbf{U}_i^n + \Delta t^n \mathcal{L}(\mathbf{U}_i^n); \\ \mathbf{U}_i^{n+1} &= \frac{1}{2}\mathbf{U}_i^n + \frac{1}{2}\mathbf{U}_i^{(1)} + \frac{1}{2}\Delta t^n \mathcal{L}(\mathbf{U}_i^{(1)}) \end{aligned}$$

where $\mathcal{L}(\mathbf{U})$ is the spatial operator from (7) and Δt^n denoted the time-step.. It is noted that, the friction and drag term treatment is implemented at the end of each RK step. The stability of the numerical scheme is imposed by the usual CFL condition for explicit schemes and the time-step Δt^n is adaptively computed from it as

$$\Delta t^n = \text{CFL} \cdot \frac{\Delta x}{\max_i \{C_{i+1/2}\}}$$

where $C_{i+1/2}$ is compute as in Section 3.1 for each I_i computational cell. The CFL value was set to 0.4 in all the computations performed in the next section, unless otherwise stated.

4 Numerical tests and solutions

In this section we present numerical tests and results to verify the ability of the proposed numerical scheme to approximate the SSWE model and the phenomena it aims to describe. More precisely, our main interested is for approximating non-stationary hydraulic jumps over constant and non-constant topographies which exhibit an oscillatory behavior in their toes and free surface. Further, and of equal importance, a family of exact solutions to the stationary SSWE is also derived.

4.1 Hydraulic jumps with different Froude numbers

These test cases were presented in [21] and are used here as to show the ability of the numerical scheme to reproduce the expected (non-stationary) behavior for non-stationary hydraulic jumps on a flat bottom. The hydraulic jump features depend on the upstream (of the jump) average Froude number (Fr_1). As it was demonstrated in [21], the jump toe (with position $x_1(t)$) oscillates for all Froude numbers greater than ~ 1.5 . The main frequency of the oscillations decreases as Fr_1 increases while the oscillation amplitude increases.

In the cases presented here we consider a channel of length $L = 10$ m and given the values for ϕ_s , C_f and C_r , supercritical inflow conditions, at $x = 0$ m, are imposed by setting $h(0, t) = h_0$ m, $q(0, t) = q_0$ m²/s and $\Psi(0, t) = 0$. At $x = L$ subcritical boundary conditions are obtained by imposing a blockage by a sharp-crested weir of height d_w with the flow given by the empirical relation [12]

$$q(L, t) = f(h) = \begin{cases} 0 & \text{if } h \leq d_w; \\ \frac{2}{3} C_d \sqrt{2g(h - d_w)^3} & \text{if } h > d_w, \end{cases} \quad (9)$$

where the discharge coefficient C_d is given by

$$C_d = \frac{\pi}{\pi + 2} + 0.08 \frac{h - d_w}{d_w}.$$

To compute the numerical flux $\mathbf{F}(\mathbf{U})_{N+1/2} = \mathbf{F}(\mathbf{U}_N^*)$ at the outflow boundary cell N we need to estimate the \mathbf{U}_N^* values as a function of \mathbf{U}_N . From (9), the discharge value is set to

$$q_N^* = f(h_N).$$

The second condition stems from the fact that Φ_N is the Riemann invariant transported by the flow at the boundary $x = L$ which give

$$\Psi_N^* = \Psi_N.$$

Finally, the water depth h_N^* is computed by the outgoing characteristic as

$$u_N - u_N^* + \int_{h_N^*}^{h_N} \frac{\sqrt{gh + 3(\phi_s + \Psi_N)h^2}}{h} dh = 0.$$

The initial condition for h given in these test cases corresponds to the approximate description of the hydraulic jump by the SWE based on the famous Bélanger formula of sequential depths which results to

$$h(x, 0) = \begin{cases} h_0 & \text{if } x \leq \frac{L}{10}; \\ \frac{1}{2} h_0 \left(-1 \sqrt{1 + 8Fr_0^2} \right) & \text{if } x > \frac{L}{10}, \end{cases} \quad (10)$$

where $Fr_0 = q_0 / \sqrt{gh_0^3}$ is the inflow Froude number. The rest of the initial conditions are $q(x, 0) = q_0$ and $\Phi(x, 0) = \phi_s$. In Figure 4.1 a schematic view of a hydraulic jump, of length L_r , forming in a wide rectangular channel is presented. The location of the jump is controlled by the downstream weir.

Following from [21], Table 1 gives the parameters values used for three test cases. Table 2 gives the target values for water depth h^* and large-scale enstrophy Ψ^* , upstream of the jump as derived by the Rankine-Hugoniot relations corresponding to the three balance equations for a stationary shock in a horizontal channel, with h_2 being the depth at the end of the roller length L_r . The roller length can be estimated by the experimentally established empirical law [11]

$$L_r = h_1 160 \tanh \left(\frac{Fr_1}{20} \right) - 12h_1, \quad 2.5 < Fr_1 < 16. \quad (11)$$

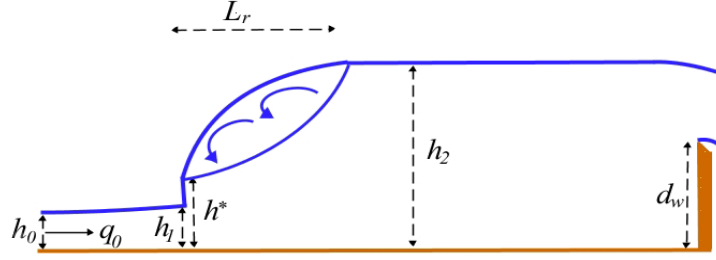


Figure 4.1: Schematic view of a hydraulic jump on a flat bed controlled by a downstream weir of height d_w

| Case | HJ2 | HJ3 | HJ4 |
|------------------|---------|---------|---------|
| Average Fr_1 | 2.0 | 5.56 | 11.25 |
| $q_0(m^2/s)$ | 0.0835 | 0.02286 | 0.0835 |
| $h_0(m)$ | 0.05 | 0.011 | 0.016 |
| C_f | 0.00177 | 0.00236 | 0.00177 |
| C_r | 0.174 | 0.682 | 1.74 |
| $\phi_s(s^{-2})$ | 0.87 | 4.09 | 2.76 |
| $d_w(m)$ | 0.026 | 0.0344 | 0.135 |

Table 1: Test cases of non-stationary hydraulic jumps on a flat bed: parameter values used

For the numerical results presented in this section, a relative fine grid is used of $N = 2000$ grid points as to capture the fine features of the oscillatory nature of the hydraulic jumps. Figure 4.2 presents the numerical results for case HJ2 for the water depth, h , and $\Phi = \Psi + \phi_s$. The numerical solution for h is compared with the stationary profile obtained, assuming $q = uh = cst$, by (numerically) solving the system of ODES

$$h' = \frac{-C_f q^2 + 2C_r \Psi q^2 / \Phi}{gh^3 + 3\Phi h^4 - q^2}; \quad (12)$$

$$\Psi' = \frac{-2C_r \Psi q^2}{\Phi h^5}, \quad (13)$$

that depends only on the upstream given data while the numerical solution is that of the initial boundary value equations (2). Figure 4.3 presents the oscillations of the jump toe position x_1 around its average value with a frequency of $\sim 1.1Hz$ and amplitude ~ 0.045 m. These results are in almost perfect agreement with those presented in [21].

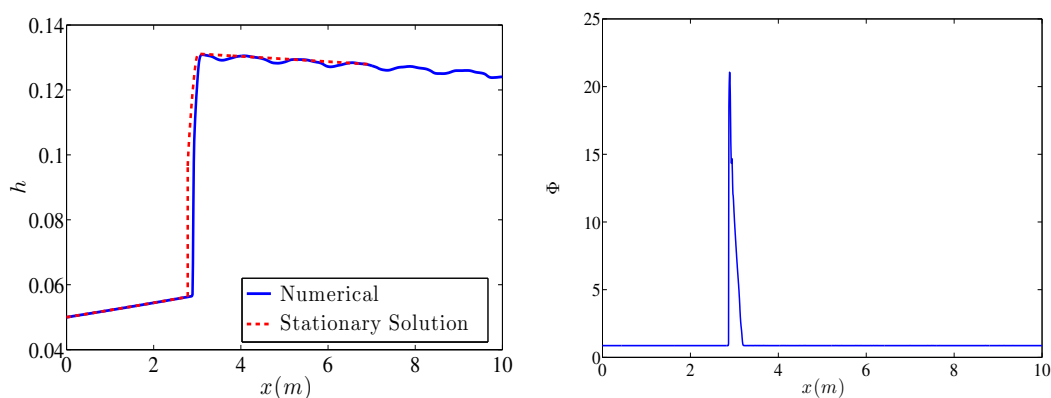
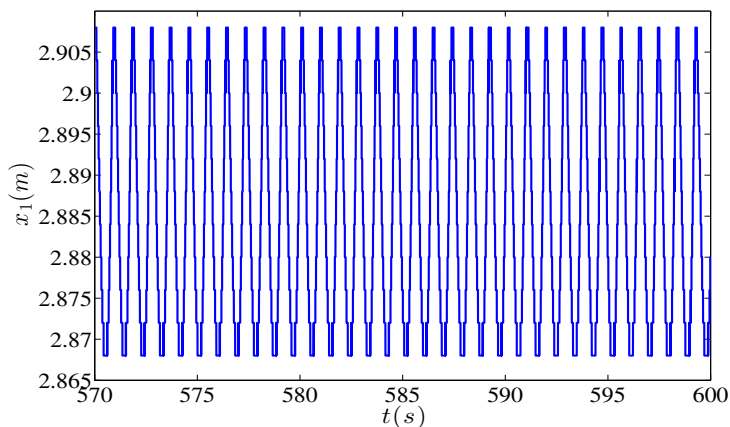
Next, and in Figures 4.4 and 4.5 the results for test case HJ3 are presented. The comparison between the water heights obtained by the numerical solution and that of the stationary profile is presented for a zoom region corresponding to three times the roller length L_r after the jump. Again the jump toe oscillates around an average value with a frequency of $\sim 0.6Hz$ and amplitude ~ 0.098 m.

In Figures 4.6 and 4.7 the results for test case HJ4 are shown. The comparison between the numerical solution and that of the stationary profile is presented here for a zoom region corresponding to almost two times the roller length L_r after the jump. The jump toe oscillates around an average value with a frequency of $\sim 0.227Hz$ and amplitude ~ 0.28 m.

Finally, in Table 3 the numerical values obtained for the target values in all three cases are

| Case | HJ2 | HJ3 | HJ4 |
|--------------------|--------|--------|--------|
| $h_1(m)$ | 0.0562 | 0.012 | 0.0178 |
| $h^*(m)$ | 0.0966 | 0.0236 | 0.0354 |
| $h_2(m)$ | 0.1313 | 0.0852 | 0.2556 |
| Ψ^* | 23.23 | 1658.5 | 4295.5 |
| $L_r(m)$ (from 11) | 0.2218 | 0.3764 | 1.3884 |

Table 2: Test cases of non-stationary hydraulic jumps on a flat bed: target values

Figure 4.2: Numerical results at time $t = 650s$ for water depth h and total enstrophy Φ for test case HJ2Figure 4.3: Oscillations in time of the jump toe position x_1 for test case HJ2

presented along with the space width in which the toe position x_1 oscillates. For the roller length estimation, following [21], a good estimation for its end is considered to be when the large scale (roller) enstrophy $\Psi = \phi_s/2$. Comparing tables 2 and 3, it can be seen that in all

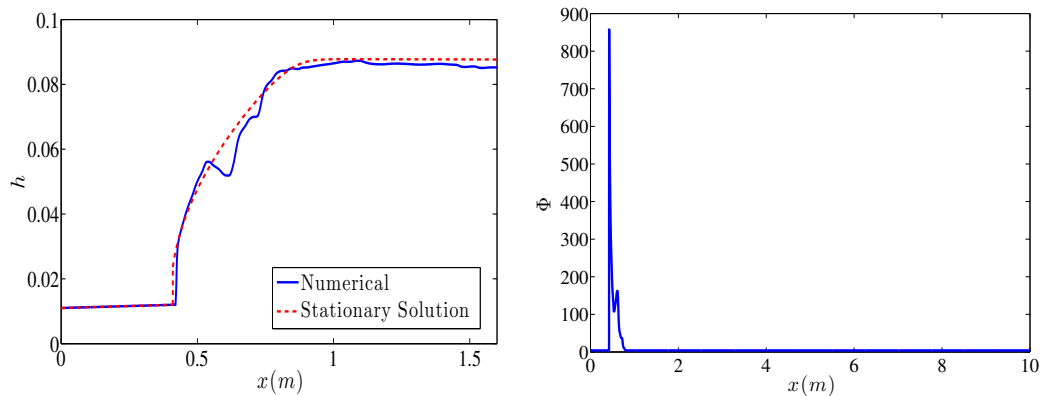


Figure 4.4: Numerical results at time $t = 550s$ for water depth h and total enstrophy Φ for test case HJ3

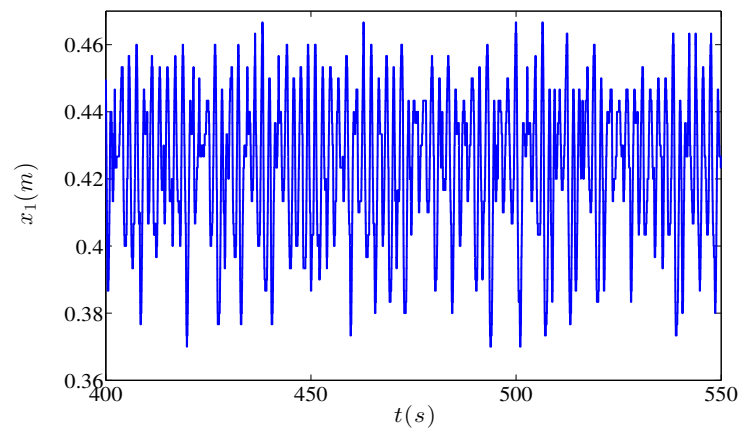


Figure 4.5: Oscillations in time of the jump toe position x_1 for test case HJ3

tests presented the expected oscillatory behavior of the hydraulic jump is demonstrated. The values of the water height obtained from the numerical simulation are very close to the ones predicted in table 2 and only the values obtained for the enstrophy Φ are underestimated for cases HJ2 and HJ3. Nevertheless, the enstrophy exhibits the correct behavior with a large and sharp increase at the jump followed by a rapid decrease after the jump and up to the end of the roller. The oscillatory nature of the jump toe position in terms of frequency and amplitude is in almost perfect agreement with the results presented in [21] for all cases.

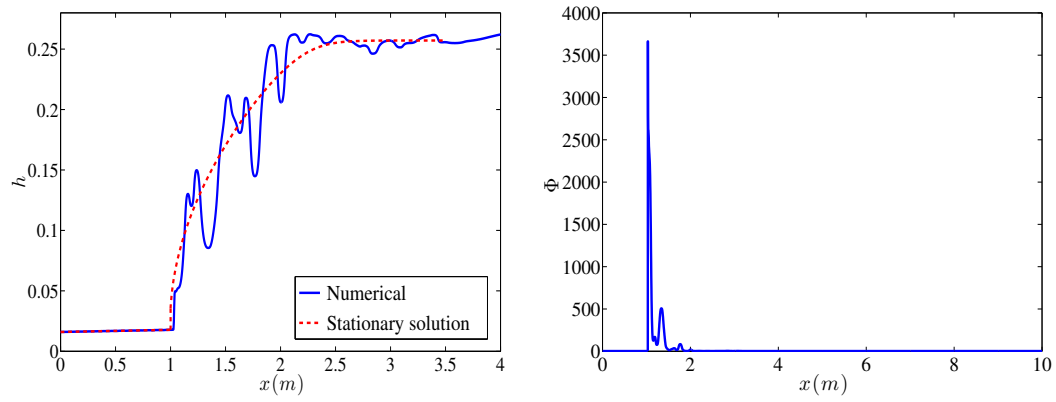


Figure 4.6: Numerical results at time $t = 350s$ for water depth h and total entrophy Φ for test case HJ4

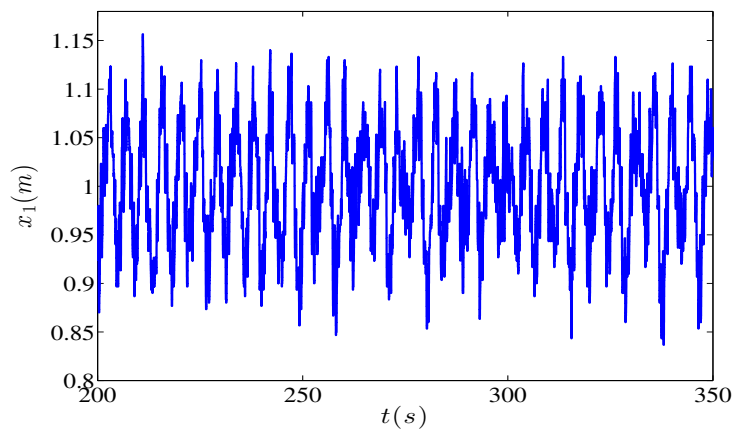


Figure 4.7: Oscillations in time of the jump toe position x_1 for test case HJ4

| Case | HJ2 | HJ3 | HJ4 |
|----------|---------------|----------------|--------------|
| $h_1(m)$ | 0.0565 | 0.0118 | 0.0181 |
| $h^*(m)$ | 0.09862 | 0.0268 | 0.0383 |
| $h_2(m)$ | 0.1308 | 0.0877 | 0.2588 |
| Ψ^* | 21.4 | 855 | 3580 |
| $L_r(m)$ | 0.215 | 0.38 | 1.46 |
| $x_1(m)$ | [2.868, 2.91] | [0.367, 0.465] | [0.85, 1.13] |

Table 3: Test cases of non-stationary hydraulic jumps on a flat bed: numerical simulations

4.2 Modified benchmark test problems of [16]

Our aim here is to construct some analytical solutions to the steady SSWE over varying topography. Although these solutions are not for oscillatory hydraulic jumps (since their corresponding Froude numbers is less than 2) their validity is of importance since they can serve as benchmark solutions to the model equations and numerical schemes. In [15, 16, 17], a set of realistic steady open channel flow test cases with analytic solution are given for the Saint-Venant equations. These test problems are often used for code benchmarking and comparison, we refer for example in [7, 8, 1, 23, 13, 14, 19, 6, 2] among others. Two such cases from [15, 16, 17] are utilized and modified here.

We first recall how these analytic solutions are constructed for the SWE by looking for steady piece-wise smooth solutions of the SWE characterized by a constant discharge q . Each smooth part of a solution is connected by a hydraulic jump. On each smooth part of the solution, the momentum equation becomes

$$[1 - Fr^2]h' + C_f Fr |Fr| = -b' \quad (14)$$

Let x_* be a point of discontinuity of the solution, the solution h_L on the left side of the discontinuity is arbitrary chosen and (14) is used to deduce the left bed slope b' :

$$[1 - Fr^2(h_L)]h'_L + C_f Fr(h_L)|Fr(h_L)| = -b'_L \quad (15)$$

By deriving relation (15), we can also compute the successive left derivatives of the bed in x_* : $b'_L(x_*)$, $b''_L(x_*)$, \dots , $b^{(n)}_L(x_*)$. Then the Rankine-Hugoniot relation is used to deduce the water height h_R^* on the right side of the discontinuity. The form of the right solution $h_R(x)$ is then chosen as a function defined by n free parameters. These parameters are computed by solving the algebraic system requiring that $h_R^* = h_R(x_*^R)$ and that the bed at x_* and its $n - 1$ successive derivatives are continuous. Using relation (14) and its derivatives, gives the $n - 1$ equations $b'_R(x_*) = b'_L(x_*)$, $b''_R(x_*) = b''_L(x_*)$, \dots , $b^{(n-1)}_R(x_*) = b^{(n-1)}_L(x_*)$ that together with $h_R^* = h_R(x_*^R)$ are solved for the n free parameters.

4.2.1 Supercritical flow with hydraulic jump on a varying bed

The first example of analytic solutions constructed with this strategy is adapted from the Example 4 of [16]. This concerns a 1km long channel with a $q = 2 \text{ m}^2/\text{s}$ discharge. The flow is supercritical at inflow with a water depth of $h_0 = 0.543853 \text{ m}$, it experiences an hydraulic jump at $x^* = 500\text{m}$ and then remains subcritical. The water depth is given by the expression:

$$h(x) = \begin{cases} 0.6673794620 - 0.1235887893 e^{-0.004 x} & \text{for } 0 \leq x < 500 \\ 0.7415327355(1. + a_1 e^{-0.02 x + 10.0} + a_2 e^{-0.04 x + 20.0} + a_3 e^{-0.06 x + 30.0}) + 0.5932261883 e^{0.001 x - 1} & \text{for } 500 \leq x \leq 1000 \end{cases} \quad (16)$$

and equation (14) allows to compute the corresponding bed slope. The values of the parameters in (16) are $a_1 = -0.2935698553$, $a_2 = 0.4080344466$, $a_3 = -0.4662074787$. Note that the values of the parameters a_1, a_2, a_3 are slightly different from the values given in [16]. This is due to the fact that the friction law used in [16] is the Manning one while here the Darcy-Weisbach law with a friction coefficient $C_f = 0.0053125$ has been used. We refer in the Appendix for an explanation and the relation between the two friction formulas.

While (16) is an exact solution of the nonlinear SWE it is not an exact solution of the shear shallow water model (2). Instead of (14), steady piece-wise smooth solutions of this model are characterized by the system of equations:

$$\text{momentum} \quad [1 - Fr^2(h) + 3\Phi h/g]h' + h^2\Phi'/g + C_f Fr(h)|Fr(h)| = -b' \quad (17.a)$$

$$\text{enstrophy} \quad h^5\Phi\Phi' = -2C_r|q|q(\Phi - \phi_s) \quad (17.b)$$

The same strategy as the one used in [16] can be employed to construct analytic solutions of (2) on a varying bed. However, this would result in a bed slope different from the one corresponding to the analytic solution of the shallow water equations. As our objective is also to compare the two models, we have found more interesting to use the same definition of the bed slope (that is thus computed as in [16] by (14)) and to numerically integrate the system of ordinary differential equation (17) to get the corresponding solution for the shear shallow water model (2). For this model the values of the small scale enstrophy ϕ_s and enstrophy dissipation coefficient C_r are constant and have been computed as recommended in [20, 21]:

$$\phi_s := 0.005 \cdot g/h_L(x_*), \quad C_r := 0.0688 \cdot Fr(h_L(x_*))^{1.337}. \quad (18)$$

In this case the upstream of the jump Froude number is 1.21. Table 4 presents the values obtained by the analytical solutions of the SWE and the SSWE upstream and downstream of the jump as well as at the end of the channel for the water depth.

Figure 4.8 compares the results for water depth given by the two models on this bed slope as well as the numerical solution for the SSWE obtained with $N = 1000$ mesh points at time $t = 500$ s. For the numerical solution of the SSWE the exact solution of the SWE is given as initial condition. It is seen that up to the hydraulic jump, the two analytic solutions cannot be distinguished. This is due to the fact that the solution for the enstrophy upwind to the discontinuity location x_* is given by: $\Phi \equiv \phi_s; \Phi' \equiv 0$ that is an exact solution of (17b). Then (17a) differs from the momentum equation of the shallow water model only by the term $3\phi_s h/g$ that is never larger than 10^{-6} for $x < x_*$ ($\phi_s = 0.07538574235$). On the discontinuity, the SSW model predicts an increase of the enstrophy and a smaller jump of the water height than in the SWE model. Downwind of the jump, the enstrophy relaxes very rapidly to the value of the small scale enstrophy. This is also confirmed numerically in Figure 4.10 (left panel), although the maximum value of Φ_R is slightly underestimated. Nevertheless, the numerical solution of the SSWE for the water depth is almost identical to the analytic solution. The water height slowly increases for the two models, with the value computed by the SSW model being continuously smaller than the value given by the SWE model. Further, the well-balance property of the numerical scheme is verified numerically on the right panel of Figure 4.10 where the computed discharge is presented. Only at the position of the jump a small glitch in the expected steady solution can be observed. This is a common behavior of all well-balanced schemes that satisfy the stagnant water well-balanced property.

| | h_L | h_R | Φ_L | Φ_R | $h(1000)$ |
|------|--------------|--------------|----------|----------|-----------|
| SWE | 0.6506535382 | 0.8405137415 | – | – | 1.3347490 |
| SSWE | 0.6506535382 | 0.8124613430 | 0.07538 | 0.156428 | 1.1856609 |

Table 4: Comparison of exact values between the shallow water model (SWE) and the shear shallow water model (SSWE) for the modified Example 4 of [16]

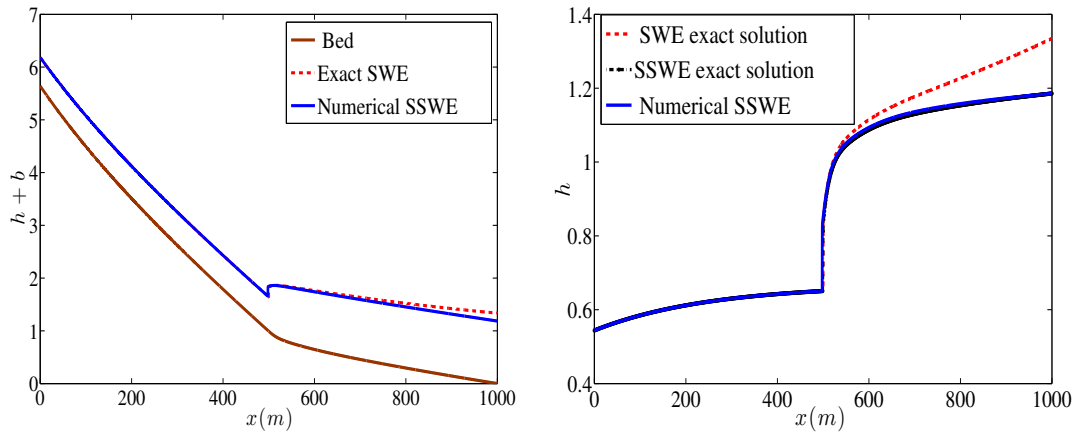


Figure 4.8: Water depth for the modified Example 4 case of [16]: Comparison between the shallow water model (SWE), the shear shallow water model (SSWE) and the numerical solution for SSWE

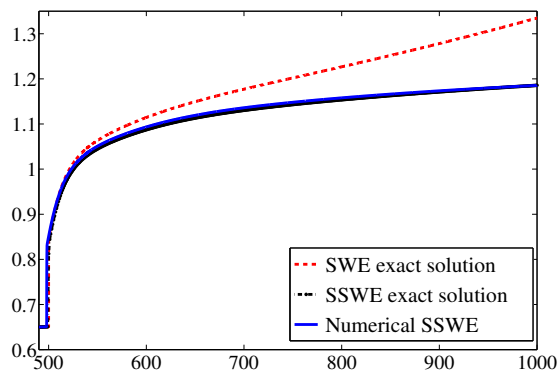


Figure 4.9: Zoomed area of water depth for the modified Example 4 case of [16]: Comparison between the shallow water model (SWE), the shear shallow water model (SSWE) and the numerical solution for SSWE

4.2.2 Flow on constant slope followed by an hydraulic jump

This test case is analogous to the one described in [15] (page 120) as problem 5. The domain is 100m long and on the left of the discontinuity, located in $x = 50$ m, water flows with a constant depth of 0.7 m on a bed of constant slope. Then the bed flattens out smoothly and creates an hydraulic jump. This test case from [15] refers to a prismatic channel and uses the Manning friction law. In order to get results close to the ones in [15] we first have to estimate the discharge. For that we estimate, from the results in [15], the jump of the water height at the

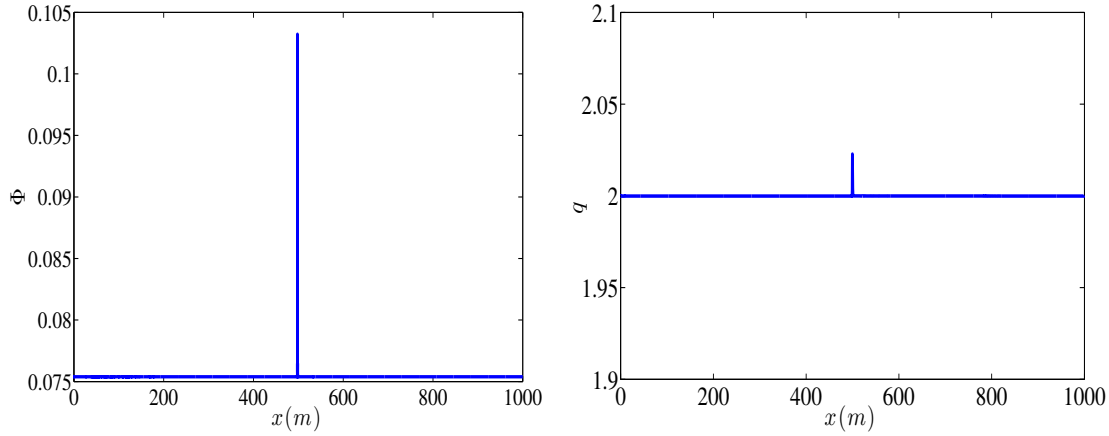


Figure 4.10: Numerical solution of the SSWE for total enstrophy (left) and discharge (right) for modified Example 4 of [16]

discontinuity from the Belanger relation

$$h_R/h_L = (\sqrt{1 + 8Fr_L^2} - 1)/2$$

which gives the jump in the water height as a function of the upwind Froude number. From that we deduce the Froude number on the left side of the discontinuity. With $h_R = 1.306421438$, this give a Froude number of 1.635459113 and a discharge of $q = 3 \text{ m}^2/\text{s}$. It remains to compute the friction coefficient of the Darcy-Weisbach law. First, from the formula given in [15] (p. 117), we compute that the constant slope on the left is $b'_L = -0.06119282892$. Then using relation (15) with $h' \equiv 0$ we deduce the friction coefficient $C_f = 0.02287816294$. Then, the water depth is given by the expression:

$$h(x) = \begin{cases} 0.7 & \text{for } 0 \leq x < 50 \\ \exp(-p(x - x_*) \sum k_i \left(\frac{x - x_*}{x_{**} - x_*}\right)^i) + \varphi(x) & \text{for } 50 \leq x \leq 100 \end{cases} \quad (19)$$

The k_0 coefficient has the value $h_R^* - 1.9 * \exp(0.0005 * (x_* - 100))$ in order for the water height on the right to be continuous while the other coefficients are given by : $k_1 = -9.314064506$, $k_2 = -73.51227688$, $k_3 = -225.0402141$, $k_4 = 359.7904991$. The bed slope profile then results from expression (14). This suffices to define the test case for the SWE model. For the SSWE model we need in addition to define the values of the small scale enstrophy and dissipation coefficient of the enstrophy. Using again the relations given in [20, 21] we obtain:

$$\phi_s := 0.005 \cdot g/h_L(x_*) = 0.07007142855, \quad C_r := 0.0688 \cdot Fr(h_L(x_*))^{1.337} = 0.1328081433. \quad (20)$$

Then, we numerically integrate the system of ordinary differential equation (17) to get the corresponding solution for the SSWE model.

Table 5 and Figure 4.11 compare the exact results for the water depth given by the two models for this bed slope as well as the numerical solution obtained for the SSWE. Again the

jump in water height obtained by the SSW model is smaller than with the plain SWE. However, on the outflow, the difference is relatively small and the difference of water height between the two models is smaller than 6cm . Again, the enstrophy relaxes very rapidly to its pre-shock value, as shown also in Figure 4.12 (left panel) that displays its numerical solution along with the computed discharge.

| | h_L | h_R | Φ_L | Φ_R | $h(100)$ |
|------|-------|-------------|-------------|-------------|-------------|
| SWE | 0.7 | 1.306421438 | - | - | 1.900000001 |
| SSWE | 0.7 | 1.100077788 | 0.070071428 | 0.876972679 | 1.843596552 |

Table 5: Comparison of exact values between the shallow water model (SWE) and the shear shallow water model (SSWE) for the modified Problem 5 of [15]

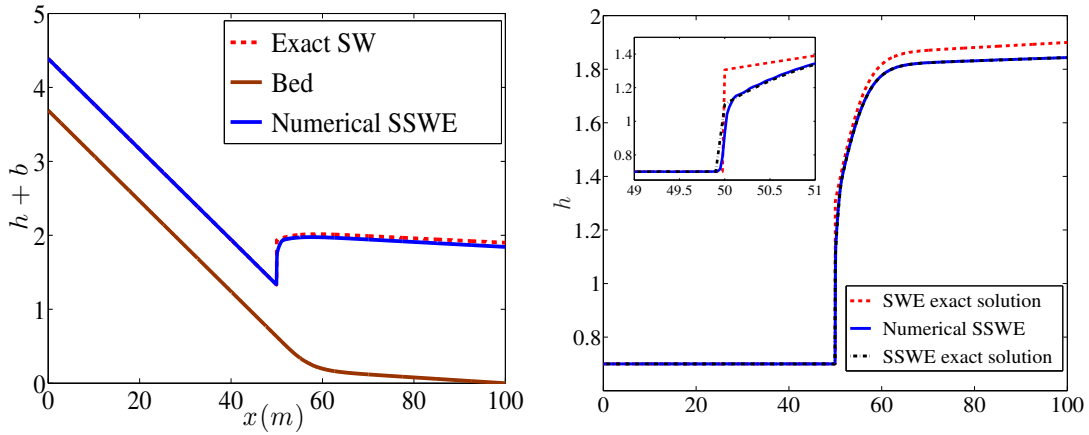


Figure 4.11: Water Depth for Example 5 case of [16]: Water depth for the modified Problem 5 of [15]: Comparison between the shallow water model (SWE), the shear shallow water model (SSWE) and the numerical solution for SSWE

4.3 Flow over a parabolic bump-transcritical flow with a shock

Here we present a modification of a classical test case, from [9], frequently used to assess the performance of well-balanced shock-capturing numerical schemes for approximating steady-state solution for the SWE with topography. If bottom friction is not considered, an analytic solution is available for testing the water level calculations for the SWE. Here, we aim to present the numerical solution obtained by solving the SSWE with all source terms present and assess its behavior. In this test case, the domain length is $L = 25\text{ m}$ with a topography given by:

$$b(x) = \begin{cases} 0.2 - 0.05(x - 10)^2 & \text{if } 8\text{m} < x < 12\text{m}, \\ 0 & \text{else} \end{cases}.$$

We choose for initial conditions

$$h(x, 0) + b(x) = 0.33\text{ m} \quad \text{and} \quad q(x, 0) = 0\text{ m}^2/\text{s}$$

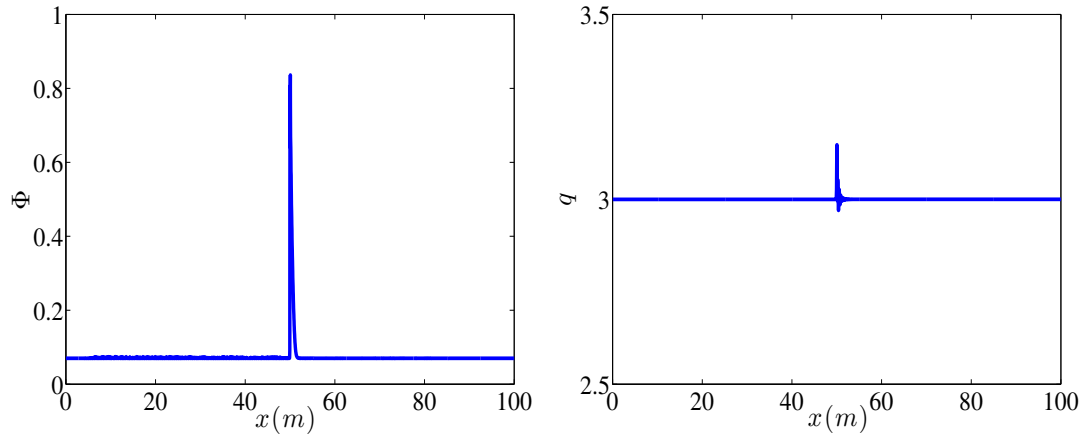


Figure 4.12: Numerical solution of the SSWE for total entrophy (left) and discharge (right) for modified Problem 5 of [15]

and the following boundary conditions

$$\begin{cases} \text{upstream : } q = 0.18m^2/s, \\ \text{downstream : } h = 0.33m \end{cases}$$

Due to the steep change in bed elevation, the flow changes from subcritical to supercritical and back to subcritical.

The $C_f = f/8 = 0.001616907601743$ friction coefficient in this case was estimate following [21] by the formula [12]

$$\frac{1}{\sqrt{f}} = 2 \log_{10} (Re \sqrt{f}) - 0.8$$

where $Re = 4q/\nu$ is the Reynolds number with $\nu = 1.309 \cdot 10^{-6}$ being the kinematic viscosity. For the SSWE equations the values for $\phi_s = 0.005 * g/h_1 = 0.607129595246937$ and $C_r = 0.0688F_1^{1.337} = 0.235228180190780$. Since the values h_1 and F_1 at the jump toe were not known for the SSWE, these were based on estimates from the numerical results obtained for the SWE solution with friction. The upstream of the jump average Froude number, Fr_1 , used to obtain the above values was 2.4 thus, it is expected that the jump toe will oscillate near some average value.

In Figure 4.13 a comparison is presented between the exact SWE solution (with no friction present) and that obtained for the SSWE at $t = 200$ s using a relatively fine mesh of $N = 2000$ grid points. For the SSWE the intensity of the jump is lower compared to that of the SWE. The computed total entrophy, presented in Figure 4.14 (left panel), exhibits the expected behavior i.e. downwind of the jump the entrophy relaxes very rapidly to the value of the small scale entrophy. In Figure 4.14 (left panel) the computed discharge is given. More importantly, Figure 4.15 presents the oscillations of the jump toe position x_1 around its average value with an amplitude of ~ 0.05 m. Finally, the "theoretical" value of the roller length $L_r = 1.1035$, obtained from (11), is closely approximated by the numerical results which gives a value of 1.180.

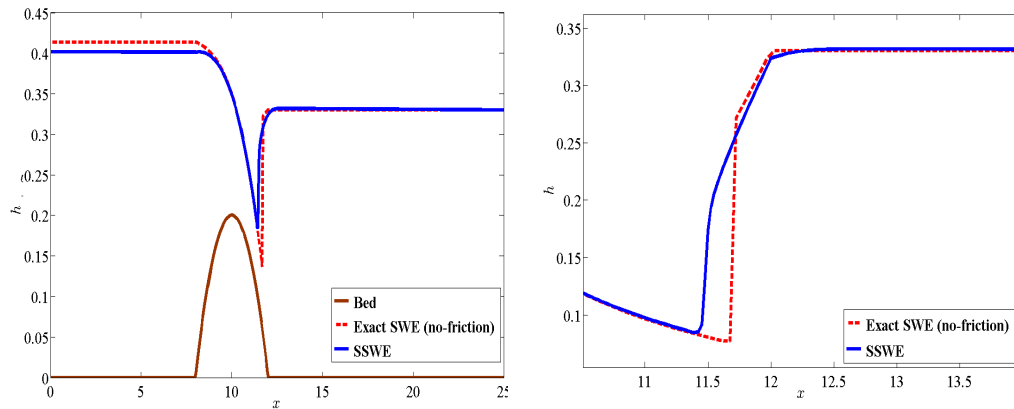


Figure 4.13: Water level and topography for the SWE and SSWE (left) and zoom at the water depth around the jump area

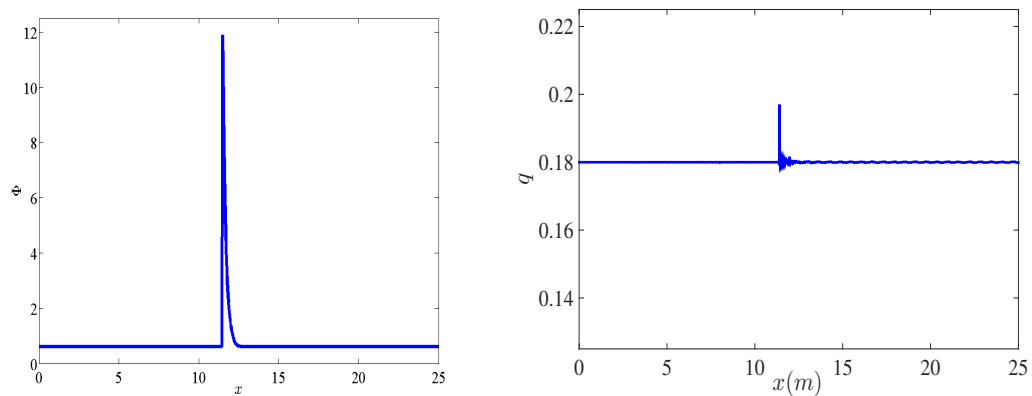


Figure 4.14: Numerical total entrophy(left) and discharge (right) for the transcritical case over a bump

4.4 Experimental forced hydraulic jump

Recently in [5] an experimental and numerical investigation was presented for the a forced hydraulic jumps on inclined beds. The main objective of this study was to assess the free surface and velocity field for a forced hydraulic jump by using non-intrusive measuring techniques as well as a mesh-free numerical method. The test case considered here is for an inclination angle of 5° in a channel of $L = 1.14$ m long.

A weir of height $d_w = 0.03$ m was placed at the downstream end of the channel. The inflow conditions consist of a discharge $q_0 = 5.608 \cdot 10^{-3} \text{ m}^2/\text{s}$ and $h_0 = 0.01$ m. The parameters used for the SSWE have been computed by the “standard” relations of Section 4.3 and are $C_r = 0.433218407749443$, $C_f = 0.003369082820920$ and $\phi_s = 8.373175770887171$ based on measured average values of $Fr_1 = 3.96$ and $h_1 = 0.005858$ at the toe of the hydraulic jump in

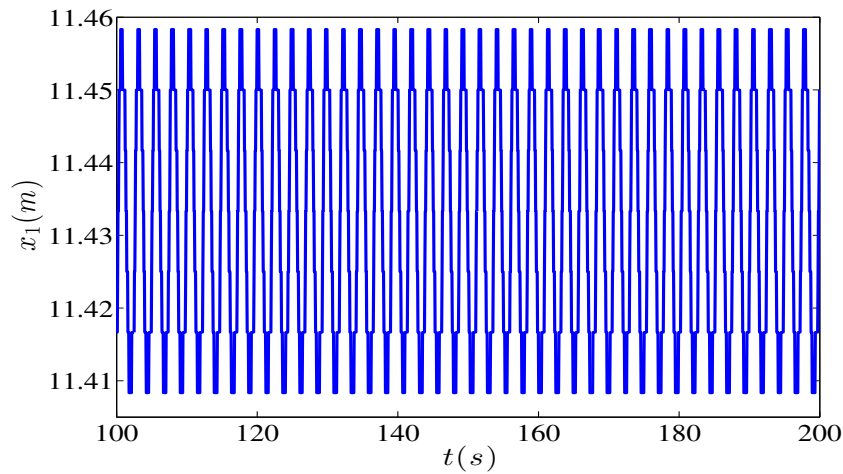


Figure 4.15: Position of the jump toe $x_1(t)$ for the flow over a parabolic hump

the experimental data. In the experiment at $t=0$, the slope is considered dry. In the numerical simulations, an artificially bed wetting with a wetting parameter of 10^{-6} was implemented [22].

In the experiments, the development of the forced hydraulic jump started after the fluid contacted the weir and a surge started to develop towards the upstream direction. This backward propagation is essential to the formation of the jumps. Eventually, the backward propagation stopped in time and it was observed that the toe of the jump continuously oscillated but the entire structure of the jumps became gradually approximately consistent. In the experiment the jump is form around $t = 4$ s. Although it cannot be excluded that in the initial stages, the flows exhibits some 3D phenomena, the agreement between the experimental results and the 2D numerical simulations reported in [5] shows that this experiment can serve as a concrete test for the 1D model considered here to test its ability to reproduce some importance features of forced hydraulic jumps.

Fig. 4.16 presents the comparison between experimental and numerical solutions obtained with the SSWE and the SWE at $t \approx 4$ s for the water depth using $N = 400$ mesh points and a reduced CFL value of 0.25. In Fig. 4.16 approximately the last 30 cm of the channel are shown since that was the area where experimental measurements were recorded and a snapshot, obtained with a high-speed camera, is also shown. As expected the SWE produce a stationary solution while the SSWE follows relatively close the experimental data at this time wich correspond to the initial formation of the hydraulic jump. Although at the initial stages the numerical model is late in describing the phenomena, also due to the artificial wetting used, the simulated jump gradually matched the experimental data. Figure 4.17 presents the total enstrophy and velocity profiles as computed by the numerical scheme. The predicted roller length was $L_r \approx 0.135$ m. Figure 4.18 presents the comparison for the free surface between the numerical and experimental data at later time instances. The shift of the jump toe is evident and the numerical solution gives a relatively accurate representation of the free surface variation. Finally, the oscillatory nature of the computed hydraulic jump is obvious from the recording of the toe position x_1 around an average value as presented in Figure 4.19.

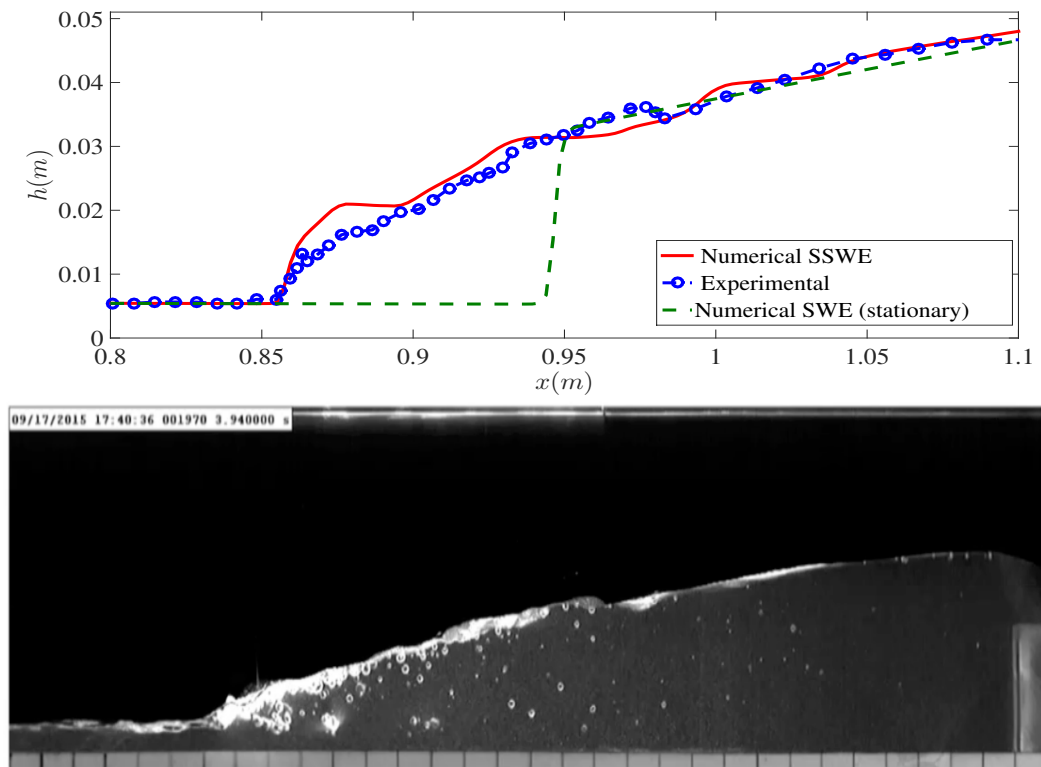


Figure 4.16: Water depth for the forced hydraulic jump experiment: comparison between numerical solution and experimental data (top) and experimental snapshot (bottom) at $t \approx 4$ s

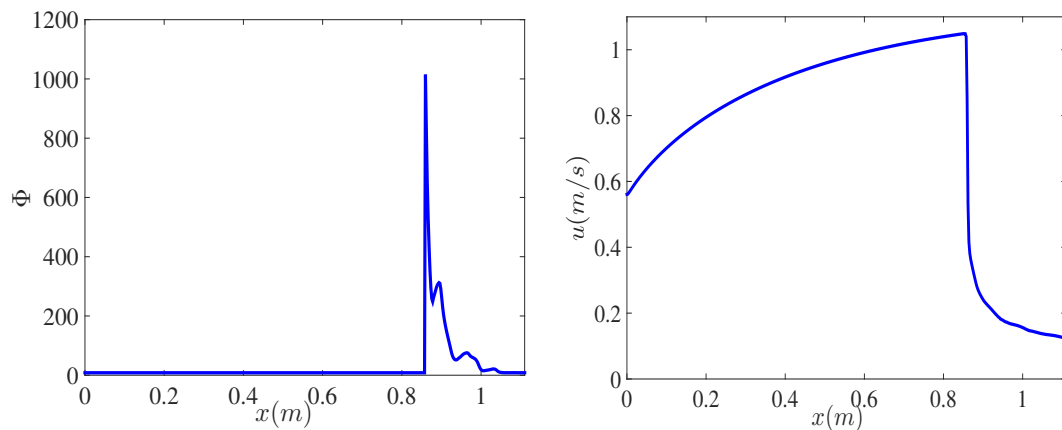


Figure 4.17: Total entrophy (left) and velocity (right) for the forced hydraulic jump experiment

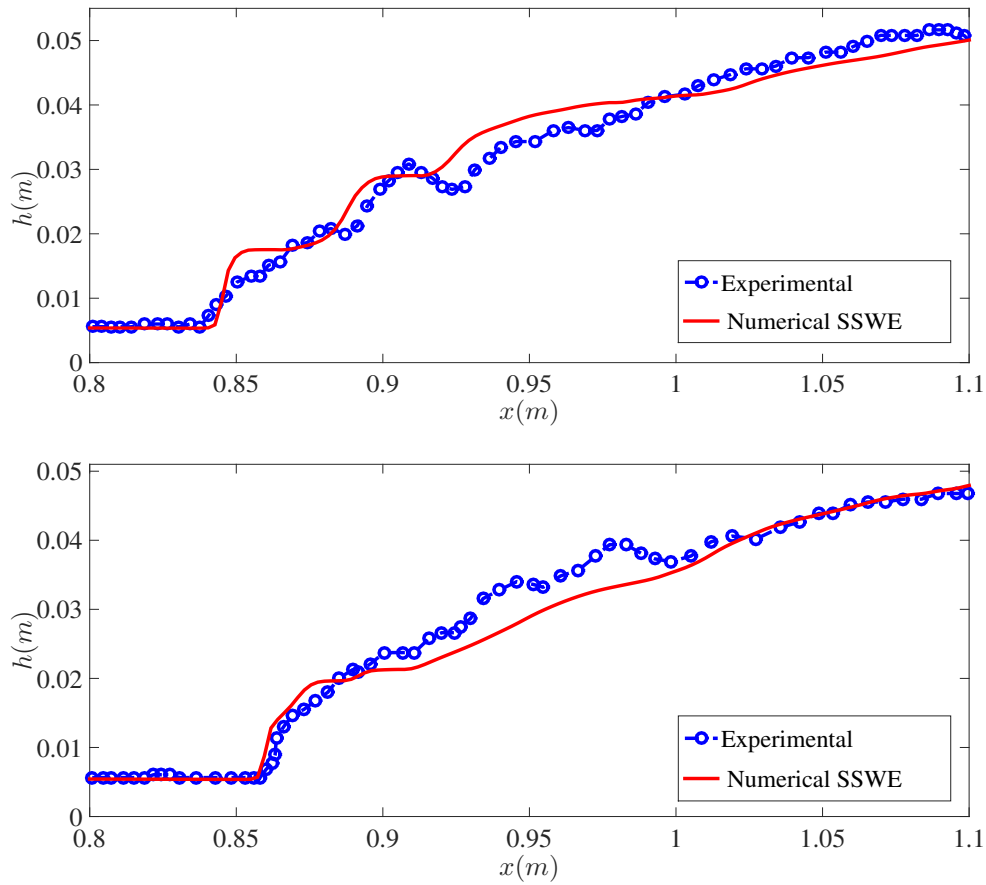


Figure 4.18: Water depth for the forced hydraulic jump experiment: comparison between numerical solution and experimental data at $t \approx 5.5$ s (top) and $t \approx 7$ s (bottom)

5 Conclusions

An extension and numerical solution of a previously developed two-parameter mathematical model describing shear shallow water flows was presented to study turbulent hydraulic jumps. The mathematical model called the shear shallow water equations (SSWE) consists in a conservative hyperbolic system with source terms defined by two parameters, the wall enstrophy and energy dissipation coefficient that have a well-defined physical interpretation. The SSWE were extended here in a straightforward manner as to incorporate arbitrary non-constant topographies without any adjustments to the model's parameters. To this end, a conservative second-order, in space and time, finite volume scheme was developed to numerically approximate the extended model. The proposed scheme satisfies the well-balance property for quiescent flows over topography. Several numerical tests were performed as to access the ability of the numerical model to predict the formation of turbulent hydraulic jumps for upstream Froude numbers larger than 1.7. The model was capable of predicting the oscillatory nature of such jumps, a phenomenon well-documented in the literature, and several characteristics such

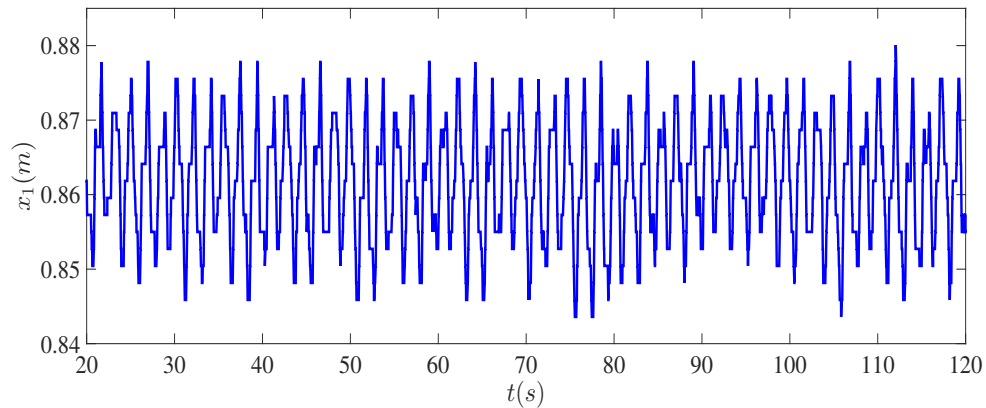


Figure 4.19: Oscillations in time of the jump toe position x_1 for the experimental forced hydraulic jump test case

as the free surface evolution and jump roller length in a very satisfactory way. Comparisons with experimental data of a forced hydraulic jump were also presented and given the 1D nature of the model, show a very good agreement with the data. Finally, another contribution of this work is the derivation of a set of new analytic steady-state solutions to the SSWE model over variable topography. These exact solutions, although not for oscillatory hydraulic jumps, can serve as benchmark solutions to the validation of any numerical scheme aiming to approximate the model equations.

Acknowledgment

This work originates from visits of Yih-Chin Tai to Inria Sophia-Antipolis and of H. Guillard to the National Center for Theoretical Sciences (NCTS) of National Tawain University in the framework of the Inria - MOST Associate team program AMoSS. H. Guillard acknowledges the warm hospitality of NCTS and of the Technical University of Crete during the completion of this work. A.I. Delis wishes to thank the INRIA - Nice Sophia Antipolis University team CASTOR for its hospitality while contracting part of the presented research. The authors would also like to thank Boniface Nkonga, Mario Ricchiuto and Sergey Gavriluk for fruitful discussions on the SSWE model and its numerical approximation.

References

- [1] J. Burguete and P. García-Navarro. Efficient construction of high-resolution TVD conservative schemes for equations with source terms: Application to shallow water flows. *International Journal for Numerical Methods in Fluids*, 37(2):209–248, 2001.
- [2] D. Caviedes-Voullième and G. Kesserwani. Benchmarking a multiresolution Discontinuous Galerkin shallow water model: Implications for computational hydraulics. *Advances in Water Resources*, 86:14–31, 2015.

- [3] Y. Chachereau and H. Chanson. Free-surface fluctuations and turbulence in hydraulic jumps. *Experimental Thermal and Fluid Science*, 35:896–909, 2011.
- [4] H. Chanson. Convective transport of air bubbles in strong hydraulic jumps. *Int. J. Multiphase Flow*, 36:798–814, 2010.
- [5] C.-K. Cheng, Y.-C. Tai, and Y.-C. Jin. Particle image velocity measurement and mesh-free method modeling study of forced hydraulic jumps. *Journal of Hydraulic Engineering*, 143(9):to appear, 2017.
- [6] O. Delestre, C. Lucas, P.-A. Ksinant, F. Darboux, C. Laguerre, T.-N.-T. Vo, F. James, and S. Cordier. SWASHES: A compilation of shallow water analytic solutions for hydraulic and environmental studies. *International Journal for Numerical Methods in Fluids*, 72:269–300, 2013.
- [7] A.I. Delis and C.P. Skeels. TVD schemes for open channel flow. *International Journal for Numerical Methods in Fluids*, 26(7):791–809, 1998.
- [8] A.I. Delis, C.P. Skeels, and S.C. Ryrie. Implicit high-resolution methods for modelling one-dimensional open channel flow. *Journal of Hydraulic Research*, 38(5):369–381, 2000.
- [9] Maurel F. Goutal N. Proceedings of the 2nd workshop on dam-break wave simulation. Technical Report HE-43/97/016/B, Département Laboratoire National d’Hydraulic, Groupe Hydraulic Fluviale Electricité de Fracne, France, 1997.
- [10] W.H. Hager and R. Bremen. Classical hydraulic jump: sequent depths. *J. Hydraul. Res.*, 27:565–585, 1989.
- [11] W.H. Hager, R. Bremen, and N. Kawagoshi. Classical hydraulic jump: length of roller. *J. Hydraul. Res.*, 28:591–608, 1990.
- [12] F.M. Henderson. *Open Channel Flow*. MacMillan, 1966.
- [13] G. Kesserwani, R. Ghostine, J. Vazquez, A. Ghenaim, and R. Mosé. Application of a second-order Runge-Kutta discontinuous Galerkin scheme for the shallow water equations with source terms. *International Journal for Numerical Methods in Fluids*, 56(7):805–821, 2008.
- [14] S.-H. Lee and N.G. Wright. Simple and efficient solution of the shallow water equations with source terms. *International Journal for Numerical Methods in Fluids*, 63(3):313–340, 2010.
- [15] I. MacDonald. *Analysis and computation of steady open channel flows*. PhD thesis, University of Reading, 1996.
- [16] I. MacDonald, M.J. Baines, N.K. Nichols, and P.G. Samuels. Steady open channel test problems with analytic solutions. Technical Report 3/95, University of Reading, 1995.
- [17] I. MacDonald, M.J. Baines, N.K. Nichols, and P.G. Samuels. Analytic benchmark solutions for open-channel flows. *Journal of Hydraulic Engineering*, 123(11):1041–1044, 1997.
- [18] K. M. Mok. Relation of surface roller eddy formation and surface fluctuation in hydraulic jumps. *Journal of Hydraulic Research*, 42(2):207–212, 2004.
- [19] M. Morales-Hernandez, P. García-Navarro, and J. Murillo. A large time step 1d upwind explicit scheme (CFL>1): Application to shallow water equations. *Journal of Computational Physics*, 231(19):6532–6557, 2012.

- [20] G. L. Richard and S. L. Gavriluyk. A new model of roll waves: comparison with brock's experiments. *Journal of Fluid Mechanics*, 698:374–405, 004 2012.
- [21] G. L. Richard and S. L. Gavriluyk. The classical hydraulic jump in a model of shear shallow-water flows. *Journal of Fluid Mechanics*, 725:492–521, 005 2013.
- [22] E.F. Toro. *Shock-Capturing Methods for Free-Surface Shallow Flows*. John Wiley and Sons, Ltd, 1998.
- [23] M.-H. Tseng. Improved treatment of source terms in TVD scheme for shallow water equations. *Advances in Water Resources*, 27(6):617–629, 2004.

Appendix

In [15, 16, 17] the derived analytical solution are for the Saint-Venant (SV) equations for prismatic channels and in terms on the Manning friction formula. Hence, a connection between the SV equations and SWE also in terms of the Darcy-Weisbach (DW) is given here. Considering a prismatic rectangular channels with constant width B , wetted cross-sectional area $A = Bh$, wetted perimeter $P = B + 2h$ and constant discharge $Q = Au = Bhu = Bq$ the resulting SWE with topography and friction are given as

$$\frac{\partial h}{\partial t} + \frac{\partial q}{\partial x} = 0 \quad (21)$$

$$\frac{\partial q}{\partial t} + \frac{\partial}{\partial x} (q^2/h + gh^2/2) = -gh(\partial_x b - S_f^M) \quad (22)$$

where the friction slope in terms of the Manning coefficient is given as

$$S_f^M = \frac{Q|Q|n_m^2 P^{4/3}}{A^{10/3}} = \frac{Q|Q|n_m^2 (B + 2h)^{4/3}}{Bh^{10/3}} = \frac{q|q|n_m^2 (1 + \frac{2h}{B})^{4/3}}{h^{10/3}} \quad (23)$$

that is, if it is to represent the friction term coming from SV to SWE it should be with a modified friction constant

$$\tilde{n}_m^2 = n_m^2 \left(1 + \frac{2h}{B}\right)^{4/3}. \quad (24)$$

This may be expanded assuming $B \gg h$ as

$$\tilde{n}_m^2 = n_m^2 \left(1 + \frac{4}{3} \frac{2h}{B} + \frac{2}{9} \left(\frac{2h}{B}\right)^2 + \dots\right)$$

To get a global (in all the channel) estimate for \tilde{n}_m from n_m the critical depth can used i.e. from $Fr = u/\sqrt{gh} = 1$ resulting in

$$h_{cr} = \left(\frac{q^2}{g}\right)^{1/3}.$$

Thus, for the SWE the Manning friction slope maybe written as

$$S_f^M = \frac{q|q|\tilde{n}_m^2}{h^{10/3}} = \frac{u|u|\tilde{n}_m^2}{h^{4/3}} \quad (25)$$

Since in the SSWE the DW formula is used i.e.

$$S_f^{DW} = f \frac{q|q|}{8gh^3} = f \frac{u|u|}{8gh} \quad (26)$$

we can approximate f from Manning's formula above as

$$f \approx \frac{8g\tilde{n}_m^2}{h^{1/3}} \quad (27)$$

In the SSWE derivation we use in the momentum equation

$$-ghS_f^{DW} = -f \frac{u|u|}{8} = -C_f |u|u.$$

which results in the obtained form of S_f in (2).

The analytical solutions for the SWE derived in Section 4 for $h(x)$ and slope b' satisfy then the following relation for each friction term used

$$b' = \left(1 - \frac{q^2}{gh^3}\right) h'(x) + \frac{fq^2}{8gh^3} \quad (\text{DW formula}).$$

which corresponds to (14).



**RESEARCH CENTRE
SOPHIA ANTIPOLIS – MÉDITERRANÉE**

2004 route des Lucioles - BP 93
06902 Sophia Antipolis Cedex

Publisher
Inria
Domaine de Voluceau - Rocquencourt
BP 105 - 78153 Le Chesnay Cedex
inria.fr

ISSN 0249-6399